Localization and characterization of simple defects in finite-sized photonic crystals

Jean-Philippe Groby[1,2,*] and Dominique Lesselier[2]

[1]*Centre de Mathématiques Appliquées, UMR7641 CNRS/École Polytechnique, Route de Saclay, Palaiseau F-91128, France*

[2]*Département de Recherche en Électromagnétisme–Laboratoire des Signaux et Systèmes, UMR8506 (CNRS-Supélec-Univ Paris-Sud), Gif-sur-Yvette F-91192, France*

**Corresponding author: groby@lss.supelec.fr*

Received July 17, 2007; revised October 22, 2007; accepted October 23, 2007; posted November 2, 2007 (Doc. ID 85377); published December 14, 2007

Structured materials like photonic crystals require for optimal use a high degree of precision with respect to both position and optical characteristics of their components. Here we present a simple tomographic algorithm, based on a specific Green's function together with a first-order Born approximation, which enables us to localize and characterize identical defects in finite-sized photonic crystals. This algorithm is proposed as a first step to the monitoring of such materials. Illustrative numerical results show in particular the possibility of focalization beyond the Rayleigh criterion. © 2007 Optical Society of America

OCIS codes: 100.3190, 290.4210, 050.1950.

1. INTRODUCTION

Photonic crystals (PCs) [1,2] are periodic, dielectric, or metallic structures that possess a variety of band dispersions and bandgaps. They are found in antennas [3,4], waveguides [5], and negative refractive index materials [6] to quote a few usages. As is well known, for optimal use such structures require that both the position and the optical properties of their component materials be very precise. Though the density of states is zero within the photonic bandgap, by perturbing a single lattice site, a single mode or a set of closely spaced modes that have frequencies within this gap is permitted; e.g., a single column can be removed from the crystals or replaced by another of which the size, shape, or dielectric constant is different from the original. Properties [7–9] and modeling [10,11] of PCs have been extensively studied, though mostly for 2-D configurations, during the past two decades.

The present investigation is intended to be a first step toward monitoring the physical integrity of such structures. A low-complexity tomographic algorithm that enables us to localize and characterize simple defects consisting in either an absence of circular cylinders or a modification of the optical properties of such cylinders in finite-sized 2-D photonic crystals as proposed. Let us note that the retrieval of an absent circular cylinder could be seen as quite an academic goal in the sense that it is either a defect tailored to a particular application or a defect caused by bad handling of the PCs, which manifests itself by a large and very visible modification within the frequency range of the bandgap; yet the localization of a broken cylinder is still not a straightforward matter, and this calls for further investigation. As for the retrieval of the location and optical index of a modified cylinder, this could be of more practical interest since such a type of defect could result from mere deterioration of the PCs. Hereafter, localization and characterization of simple defects are carried out from a low-frequency excitation outside (below) the usual frequency range of the bandgap. Both the specific Green's function and the response to the low-frequency excitation of the original, intact structure (and of the damaged structure) can be calculated by means of the so-called multipole method [7,12], and they can be used to solve the inverse problem via a first-order Born approximation. The introduction of a specific Green's function directly exhibits the discrepancies between the initial configuration and the configuration with defects [13].

As background to this investigation, recent studies have also shown that the utilization of a structured embedding medium, like PCs, could lead to focusing and resolution of a tomographic inversion algorithm beyond the Rayleigh criterion [14,15]. The possibility of encountering such a phenomenon is also investigated herein.

2. FIELD (DATA) AND SPECIFIC GREEN'S FUNCTION

Let us consider a structure made of N parallel circular cylinders $\mathcal{C}^j$, identified by superscript $j \in N$, of radius R^j and of optical index η^j, located at $\mathbf{r}^j=(r^j,\theta^j)$ in the global polar coordinate system in the cross-sectional plane (this is a 2-D scattering configuration).

As indicated above, both fields and a specific Green's function (the latter being the field solution of the problem when the structure is excited by a given line source) are calculated by means of the multipole method [7,12]. Key to this approach are the local field expansions or multipole expansions in the vicinity of each cylinder in the polar coordinate system linked to that cylinder (which are derived from the application of Graf's addition theorem [16]):

$$E^e(\mathbf{r_l}) = \sum_{m=-\infty}^{\infty} [B_m^l H_m^{(1)}(kr_l) + A_m^l J_m(kr_l)]e^{im\theta_l}, \quad (1)$$

where $H_m^{(1)}$ is the first-kind Hankel function of order m, J_m is the Bessel function of order m, B_m^l are the coefficients of the scattered field by the lth cylinder, A_m^l are those of the incident field impinging upon the lth cylinder, and $\mathbf{r_l}=(r_l,\theta_l)$ are the coordinates of a point P in the polar coordinate system linked to this lth cylinder. The local incident field on the lth cylinder is generated by the actual incident field E^{inc} as well as by the fields that are scattered by all other cylinders j, $j\neq l$. Their coefficients also take the form

$$A_m^l = K_m^l + \sum_{j=1,j\neq l}^{N} \sum_{p=-\infty}^{\infty} S_{mp}^{lj} B_p^j, \quad (2)$$

where K_m^l are the coefficients of the actual incident field [either a planar incident wave in the cross-sectional plane, $K_m^l=(-i)^m \exp(-ikr^l \cos(\theta^{inc}-\theta^l)-im\theta^{inc})$, or a cylindrical wave generated by an exterior line source set parallel to the axis of the cylinder] and $S_{mp}^{lj}=H_{m-p}^{(1)}(kr_l^j)\times e^{i(p-m)\theta_l^j}$ are translation terms, (r_l^j,θ_l^j) being the coordinates of the jth cylinder in the polar coordinate system associated with the lth cylinder.

Coefficients A_m^l and B_m^l are related together via the continuity of the tangential components of the electric and magnetic fields to be imposed at the cylinder boundaries. To derive these relationships, the interior field expansion within the cylinder l is used as

$$E^l(\mathbf{r_l}) = \sum_{m=-\infty}^{\infty} [Q_m^l H_m^{(1)}(k\eta^l r_l) + C_m^l J_m(k\eta^l r_l)]e^{im\theta_l}, \quad (3)$$

where C_m^l are the coefficients of the scattered field inside the l cylinder and $Q_m^l=(\mathbf{i}/4)\chi^l J_m(k\eta^l r_l^s)e^{\mathbf{i}m\theta_l^s}$ are the coefficients of a field generated by a line source located at (r_l^s,θ_l^s) inside the cylinder l in the polar coordinate system associated with it. The presence of the interior source is indicated by the term χ^l valued to 1 when the source is present and 0 otherwise.

The continuity conditions at the boundaries are most conveniently expressed in terms of cylindrical harmonic reflection and transmission coefficients [7] as

$$B_m^l = R_m^l A_m^l + T_m^l Q_m^l,$$

$$C_m^l = T'^l_m A_m^l + R'^l_m Q_m^l. \quad (4)$$

In the above, vectors $\mathbf{B}=[B_m^l]$, $\mathbf{K}=[K_m^l]$, and $\mathbf{Q}=[Q_m^l]$, as well as matrices $\mathbf{S}=[S_{mp}^{jl}]$ and $\mathbf{R}=\mathrm{diag}\,R_m^l$ (with identical definition applying to the other reflection and transmission matrices and the other coefficients), are introduced in order to deduce from Eqs. (2) and (4) the system of linear equations in the source coefficients $\mathbf{B}$ as

$$(\mathbf{I}-\mathbf{RS})\mathbf{B} = \mathbf{RK}+\mathbf{TQ}. \quad (5)$$

Upon solving the above linear system both in the interior [using the second equation of Eq. (4)] and in the exterior, the specific Green's function is made available.

3. SIMPLE TOMOGRAPHIC ALGORITHM

From now on, one is considering a finite-sized crystal (FSC) with hexagonal symmetry, as is shown in Fig. 1. It is made of N (N will be chosen as 85 in the numerical examples) circular cylinders of the same radius R and the same optical index η. The cylinders $\mathcal{C}^j$, $j\in[1,N]$ are ordered such that $\mathcal{C}^1$ is located at the bottom left corner and $\mathcal{C}^N$ at the top right corner. The distance between the centers of the closest cylinders is denoted by d. The electric field is calculated on a circle of radius $r=20d$ (this is a rather arbitrary value; what matters is that one stays fully outside the crystal). Fields are time-harmonic, with wavelength in free space as λ, and wavenumber $k=2\pi/\lambda$. A defect is obtained either by removing the lth cylinder or by modifying its optical index, *de facto* creating a different configuration (denoted as lth DFSC).

Tomographic algorithms are usually derived from an integral formulation of the solution based on the so-called background (free-field) Green's function. Use of a specific Green's function, i.e., the solution (for a given line source) of a problem close to the one at hand, reduces the kernel of the integral. Here, since the structure of the materials that one is interested in is designed to exhibit specific properties, it is consistent to consider Green's function of the configuration associated with this structure (i.e., in the absence of defects) whenever intending to carry out structural monitoring.

A. Localization and Characterization of a Single Defect

One introduces $g(\mathbf{r},\mathbf{r_l^s})$ and $E(\mathbf{r})$ as the specific Green's function and the total electric field calculated for the FSC, and $E^l(\mathbf{r})$ as the total electric field calculated for the lth DFSC. These fields are related by the well-known Fredholm integral equation of the first kind $E^l(\mathbf{r})-E(\mathbf{r})=\int_{\mathcal{C}^l} g(\mathbf{r},\mathbf{r_l^s})k^2((\eta^l)^2-\eta^2)E^l(\mathbf{r_l^s})\mathrm{d}S$.

Then, a first-order Born approximation, whose accuracy is related to the fact that the field at the location of the defect should be weakly modified by the defect, is employed. Any mode associated with the defect, possibly leading to entrapment of the field, should be excited. Complementarily, one applies a low-frequency approximation, which requires that the radius of each cylinder be small enough with respect to the source wavelength (the reader could refer to Section 4 to appraise, numerically

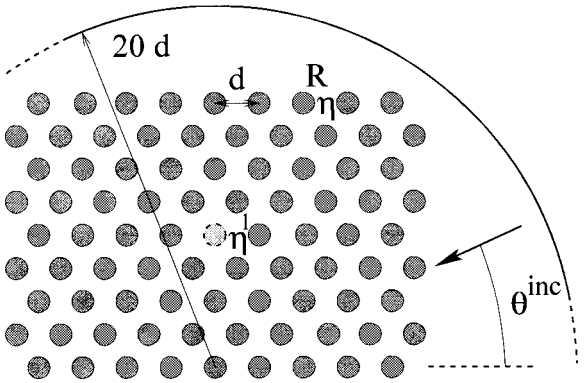

Fig. 1. Finite crystals of $N=85$ parallel circular cylinders with a single defect. The circle around the structure is the one used for the computation.

speaking, what such a definition of the radius means). Furthermore, one works outside the bandgap. Under the latter condition and for the TM polarization, the asymptotic dependencies of the coefficients of the scattered fields B_m^l and C_m^l, are $O((k\eta R)^4)$ except for $m=0$, $\forall l \in N$. The infinite sums in Eqs. (2) and (3) are reduced to their expressions at the zeroth-order term. Green's function and the field $E^l(\mathbf{r_l^s})$ can then be evaluated, under the low-frequency approximation, in quite a rigorous fashion by taking into account only the zeroth-order terms in Section 2. These quantities read as

$$g(\mathbf{r},\mathbf{r_l^s}) = \frac{iT_0}{4} J_0(k\eta r_l^s) \sum_{j=1}^{N} b_0^j(\chi^j) H_0^{(1)}(k|\mathbf{r}-\mathbf{r^j}|),$$

$$E^l(\mathbf{r_l^s}) = \mathcal{C}_{0^e}^l J_0(k\eta r_l^s) = T'_0 \mathcal{A}_{0^e}^l J_0(k\eta r_l^s). \tag{6}$$

In Eq. (6) one has introduced b_0^j, such that $(i/4)T_0 J_0(k\eta r_l^s) b_0^j = B_0^j$ is satisfying the linear set of equations $(\mathbf{I}-\mathbf{RS})\mathbf{b}=\boldsymbol{\chi}$, with vector $\boldsymbol{\chi}=[\chi^j]$. Coefficients of the locally impinging field $\mathcal{A}_0^l$ can be calculated via the solution of Eq. (2) with $\mathcal{B}_0^j$ satisfying $(\mathbf{I}-\mathbf{RS})\boldsymbol{\mathcal{B}}=\mathbf{R}\mathcal{K}$, $\mathcal{K}_0^j = e^{-ikr^j\cos(\theta^{inc}-\theta^j)}$.

By making use of relation [17] $\int x(J_0(\alpha x))^2 dx = (x^2/2)\{(J_0(\alpha x))^2+(J_1(\alpha x))^2\}$, the first-order Born approximation of the integral equation is

$$E^l(\mathbf{r}) - E(\mathbf{r}) \approx \mathcal{D}\zeta^l \mathcal{A}_0^l \sum_{j=1}^{N} b_0^j(\chi^j) H_0^{(1)}(k|\mathbf{r}-\mathbf{r^j}|), \tag{7}$$

where $\mathcal{D}=iT_0T'_0(kR)^2\{(J_0(k\eta R))^2+(J_1(k\eta R))^2\}/4$ and $\zeta^l = ((\eta^l)^2-\eta^2)$; $\mathcal{D}$ is found to be independent of both the location and the material characteristics of the defect, while ζ is the contrast function. Localization and characterization of the defect can thus be fully decoupled.

Let us introduce the normalized vector $\mathbf{v}=\mathbf{V}/\mathbf{V}\cdot\mathbf{V}^*$ ($\mathbf{V}^*$ being the complex conjugate of $\mathbf{V}$) associated with vector $\mathbf{V}=[(E^l(\mathbf{r})-E(\mathbf{r}))/\mathcal{D}]$ and N normalized vectors $\mathbf{g^j}=\mathbf{G^j}/\mathbf{G^j}\cdot\mathbf{G^j}^*$ associated with vector $\mathbf{G^j}=[\mathcal{A}_0^j \Sigma_{p=1}^N b_0^p(\chi^j) \times H_0^{(1)}(k|\mathbf{r}-\mathbf{r^p}|)]$. The defect is localized whenever $\mathcal{P}^j = |1/(1-\|z^j\|)|$, letting $z^j = \mathbf{g^j}\cdot\mathbf{v}^*/\mathbf{g^j}\cdot\mathbf{g^j}^*$, is maximum. The function $\mathcal{P}^j$ is derived from [18]. The parameter z^j corresponds to focalization at the defect location.

Finally, the optical index of the lth cylinder can be retrieved (this works quite well as seen next, yet it remains heuristic) by averaging the value of $(V(\mathbf{r})/G^l(\mathbf{r})+\eta^2)^{1/2}$ over the measured data, i.e., $\tilde{\eta}^l = \text{mean}((V(\mathbf{r})/G^l(\mathbf{r}) + \eta^2)^{1/2})$, where mean $(x(\mathbf{r}))$ means the average value of $x(\mathbf{r})$ over the measured data.

B. Localization and Characterization of Two Identical Defects

The same assumptions and procedure as above are followed for a two-identical-defect configuration, denoted as the (i,j)th DFSC configuration. The first-order Born approximation now requires that the field at the location of one defect be only weakly modified by this defect but also by the other one. This means that the defects are "well separated"; i.e., they are not interacting with each other. The approximation of the integral equation becomes

$$E^{(i,j)}(\mathbf{r}) - E(\mathbf{r}) \approx \mathcal{D}\zeta \sum_{l=1}^{N} (\mathcal{A}_0^i b_0^l(\chi^i) + \mathcal{A}_0^j b_0^l(\chi^j)) H_0^{(1)}(k|\mathbf{r}-\mathbf{r^l}|). \tag{8}$$

Similarly, with what has been done in the previous subsection, one is introducing the normalized vector $\mathbf{v}$ associated with vector $\mathbf{V}=[(E^{(i,j)}(\mathbf{r})-E(\mathbf{r}))/\mathcal{D}]$ and $N\times N$ normalized vectors $\mathbf{g^{(q,l)}}$ associated with vector $\mathbf{G^{(q,l)}} = [\Sigma_{p=1}^N (\mathcal{A}_0^q b_0^p(\chi^q) + \mathcal{A}_0^l b_0^p(\chi^l)) H_0^{(1)}(k|\mathbf{r}-\mathbf{r^p}|)]$. The defect is now localized whenever $\mathcal{P}^{(q,l)} = |1/(1-\|z^{(q,l)}\|)|$, letting $z^{(q,l)} = \mathbf{g^{(q,l)}}\cdot\mathbf{v}^*/\mathbf{g^{(q,l)}}\cdot\mathbf{g^{(q,l)}}^*$, is maximum. The optical index of the (i,j)th cylinders then follows as $\tilde{\eta}^{(i,j)} = \text{mean}((V(\mathbf{r})/G^{(i,j)}(\mathbf{r}) + \eta^2)^{1/2})$.

4. NUMERICAL RESULTS

Data are computed by use of the multipole method. The infinite sums $\Sigma_{m=-\infty}^{\infty}$ are truncated to $\Sigma_{m=-M}^{M}$ such that $M = \text{int}((k\eta R)^{1/3} + k\eta R + 5)$, where int$(x)$ is the entire part of x, which is derived from [19] with a security factor equal to 5. For the inverse problem, one does not make use of the fact that the scattered field is isotropic for the calculation of the specific Green's function as it is proposed in [12] in the low-frequency approximation. The latter is calculated directly by multiplying the vector $\mathbf{b}$ by a matrix $\mathbf{H}=[H_0^{(1)}(k|\mathbf{r}-\mathbf{r}^j|)]$, which is stored once. In the same fashion, the available asymptotic formulas of the reflection and transmission coefficients are not employed; the formulas of these coefficients are as in [7]. At this stage, to give an idea of what a radius small enough with respect to the source wavelength means, let us consider the formulas providing M. The low-frequency approximation implies that M is reduced to 0, i.e., $(k\eta R)^{1/3} + k\eta R < 1$, without a security factor. This condition is achieved for $k\eta R < 0.31$. A radius small enough with respect to the source wavelength consequently is as a first approximation a radius that satisfies $R < (0.31\lambda)/(2\pi\eta)$.

The wavelength and the optical index η are set to $\lambda = 20$ and $\eta = 2.9$, respectively. In the following, one assumes that $R=0.15$ (a value that satisfies the criterion $k\eta R < 0.31$ and also ensures that the low-frequency approximation is valid), and one mostly investigates the localization and characterization of defects located in the central part of the PCs when $\pi/2$.

Figure 2 shows $\mathcal{P}^j$ for a 43rd DFSC, with $\eta^j = 1$ (i.e., the 43rd cylinder is removed) and $\theta^{inc} = \pi/2$ when $d=4$ $(R/d = 3.75\times 10^{-2})$ and $d=1$ $(R/d = 0.15)$. In both cases, the modified cylinder is clearly retrieved and η^j is found with a relative error on its real part $Er = (\Re(\tilde{\eta}^j) - \eta^j)/\eta^j$ of less than 0.1. The 43rd cylinder seems (in the sense that the function $\mathcal{P}^l$ does not point to another cylinder) to be retrieved with an accuracy of d that is much smaller than the Rayleigh criterion $\lambda/2 = 10$.

However, this is due partly to the representation chosen; i.e., the value of $\mathcal{P}^l$ is very large since $\|z^l\| \approx 1$, with focusing beyond the Rayleigh criterion playing its part only to some extent. Indeed, strictly speaking, superresolution would mean that the width at half-height of $\|z^j\|$ is (significantly) smaller than half a wavelength. A cut of $\|z^j\|$ along the axis passing through $\mathbf{r^{43}}$ with an angle of $\pi/6$ is

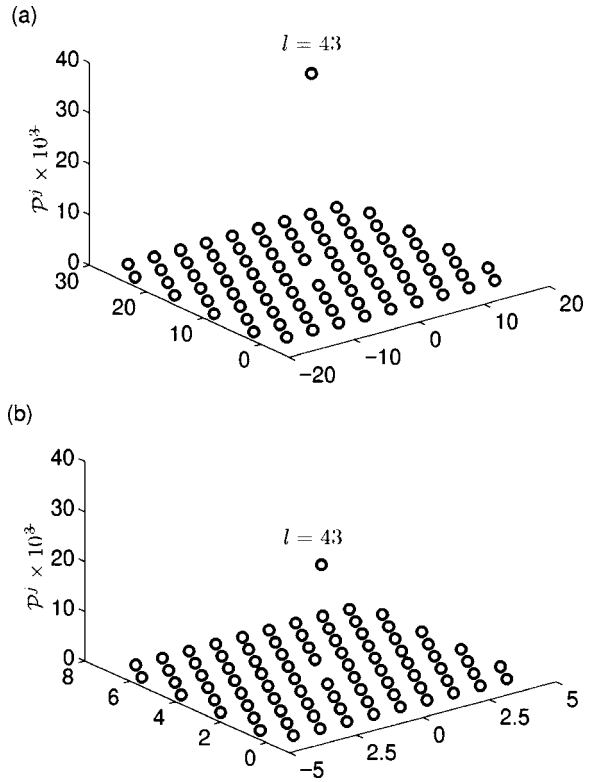

Fig. 2. Crystal with a single defect: $R=0.15$, $\eta^{43}=1$, and $\theta^{inc}=\pi/2$. (a) $\mathcal{P}^j\times10^{-3}$ when $d=4$ ($\tilde{\eta}^{43}=1.1$); (b) $\mathcal{P}^j\times10^{-3}$ when $d=1$ ($\tilde{\eta}^{43}=1.08$).

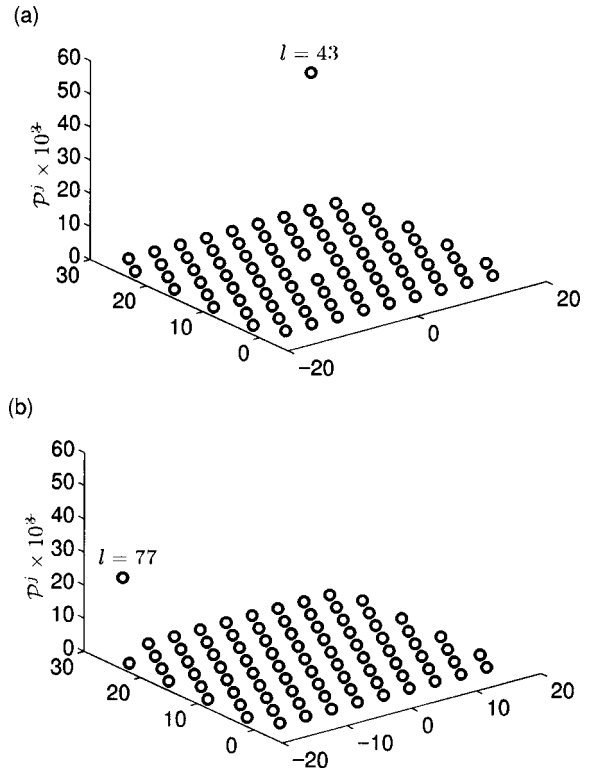

Fig. 4. Crystal with a single defect when $d=4$: $R=0.15$. (a) $\mathcal{P}^j\times10^{-3}$ when $\eta^{43}=1$ and $\theta^{inc}=\pi/4$ ($\tilde{\eta}^{43}=1.1$); (b) $\mathcal{P}^j\times10^{-3}$ when $\eta^{77}=1$ and $\theta^{inc}=\pi/2$ ($\tilde{\eta}^{77}=1.1$).

displayed in Fig. 3 for $\theta^{inc}=\pi/2$ when $d=2$ ($R/d=7.5\times10^{-2}$) and $d=1$. Superresolution, in terms of focusing accuracy, is validated in case $d=1$ and not so much in the case of $d=2$.

Let us note that the problem at hand can be interpreted as the retrieval of the location of an induced line source within a cylinder, while the problem addressed in [20] consists in the retrieval of a line source located outside all cylinders. In this sense, the problem here is quite different, but like effects are observed.

The retrieved value of $\tilde{\eta}^l$ when $d=4$ is the same when θ^{inc} is varied within $[0;\pi/2]$ as well as for a defect that is not located in the central part of the PCs, while the height of the peak of $\mathcal{P}^l$ depends on both θ^{inc} and defect location (see Fig. 4) with no obvious rule, however.

Figure 5 shows the relative error on the reconstruction of $\tilde{\eta}^{43}$ for various values of η^{43}, with $\theta^{inc}=\pi/2$ when $d=4$. The smaller the contrast ζ^l is, the better the retrieval of $\tilde{\eta}^l$ is. In particular, one is able to retrieve a $\eta^{43}=2.8$, which represents a variation of 3.45% from η, with a relative error less than 10^{-4}. The results remain accurate when the low-frequency approximation is no longer valid at the defect location yet remains valid for cylinders that are constituting the structured background.

The relative height h^l of the peak of $\mathcal{P}^l$ is defined by $h^l=\mathcal{P}^l-\text{mean}_{j\neq l}(\mathcal{P}^j)$, where $\text{mean}_j(x^j)$ is the average value of x^j over $j\in[1,N]$. The evolution of Er and of h^l with $R\in[7.5\times10^{-2},0.6]$ is shown in Fig. 6 with $\theta^{inc}=\pi/2$ when $d=4$ and $\eta^l=1$. It is observed that, even though the low-frequency approximation does not hold for the back-

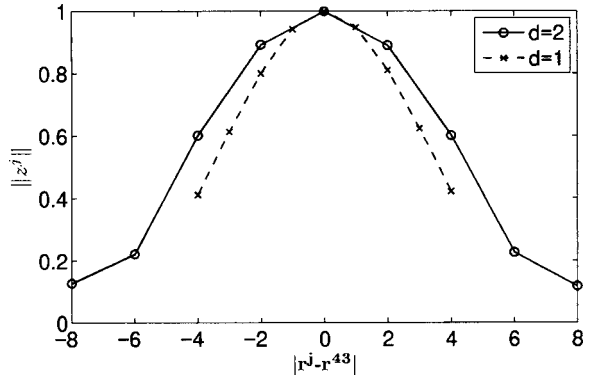

Fig. 3. Crystal with a single defect: $R=0.15$, $\eta^{43}=1$, and $\theta^{inc}=\pi/2$. Cut of $\|z^l\|$ along the axis going through $\mathbf{r}^{43}$ with an angle $\theta=\pi/6$.

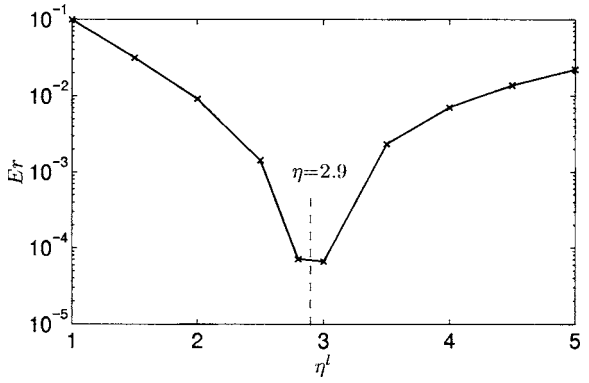

Fig. 5. Crystal with a single defect when $d=4$: $R=0.15$ and $\theta^{inc}=\pi/2$. Relative error on the reconstructed value $\tilde{\eta}^{43}$ for various η^{43}. The modified cylinder is systematically retrieved.

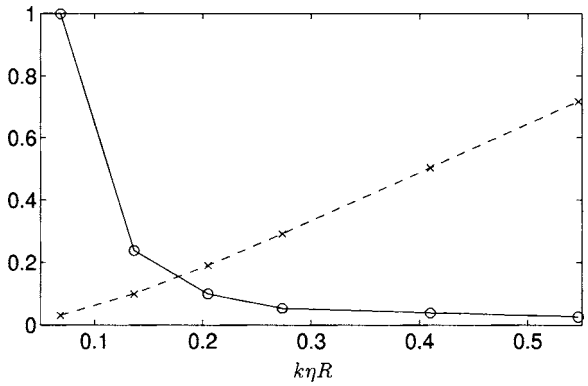

Fig. 6. Crystal with a single defect when $d=4$: $\eta^l=1$ and $\theta^{inc}=\pi/2$. Evolution of Er (dashed line) and of the height of the peak of $\mathcal{P}^l$ normalized by its value for $R=0.075$ (solid curve) for various values of R.

ground, the modified cylinder is retrieved, but the reconstructed values $\tilde{\eta}^l$ are not accurate anymore. When η is varied, the reconstructed values (in particular the imaginary part) of η^l are now inaccurate even for $k\eta R=0.27$. This means that the result, and as a matter of fact the use of the first-order Born approximation, remains much more appropriate when R becomes large than when η becomes large.

When white Gaussian noise (signal-to-noise ratio of 50 dB) is added to both real and imaginary parts of E and E^l, the corresponding normalized vector is denoted by $\mathbf{v}_{noise}$. Both $\|\mathbf{v}_{noise}\|$ and $\|\mathbf{v}\|$ are plotted in Fig. 7. The missing cylinder is imaged, and $\tilde{\eta}^l$ is retrieved with a relative error of less than 0.1. The main impact of the addition of white Gaussian noise to the data is a decrease of h^l.

As for the (i,j)th DFSC configuration, the major difficulty is in the recovery of modified cylinders close to one another; $\mathcal{P}^{(q,l)}$ is symmetric in terms of q and l. Let us define the vector $\mathcal{Q}^q$ such that $\mathcal{Q}^q=\mathcal{Q}^l=\text{mean}_l(\mathcal{P}^{(q,l)})$, which enables us to depict the results in the same form as in the case of the (l)th DFSC configuration. Figure 8 shows both $\mathcal{P}^{(q,l)}$ and $\mathcal{Q}^q$ for a (43rd, 44th) DFSC configuration with $\theta=\pi/2$ when $d=2$. Two identically modified cylinders are retrieved, separated by a distance d which is smaller than $\lambda/2$.

Finally, let us consider more realistic parameters for the cylinders, in the usual PCs sense, with radius $R=0.6$, spacing $d=4$, and optical index $\eta=2.9$. In this case, the gap lies between wavelengths 7.3 and 10.8 [10]. The average absolute value of the electric fields is computed on a 10-large segment set at distance d below the crystal in its central region [refer to Fig. 9(a)]. When the central cylinder is removed, a sharp transmission peak shows up at wavelength $\lambda\approx 9.06$ since a resonance occurs in the resultant microcavity.

It is clear that the modification of the electric field is very large within the bandgap and that this frequency range should be taken in account for monitoring the structural integrity of PCs. Nevertheless, both the frequency and the height of the peak appear to be related to the type, location, and number of defects [10]. In practice, this indicates that monitoring for defects within the bandgap should be performed by accounting for the whole frequency over the bandgap (and not only for one single frequency), as both the low-frequency and the first-order

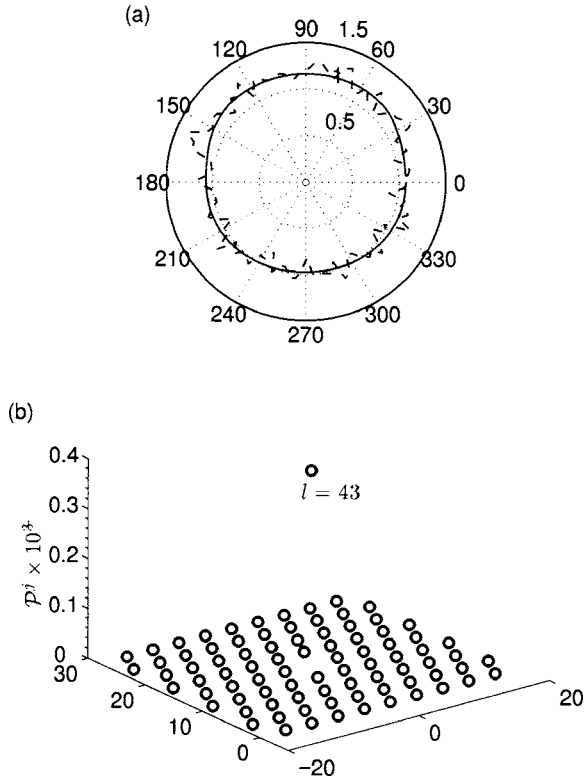

Fig. 7. Crystal with a single defect when $d=4$: $R=0.15$, $\eta^l=1$, and $\theta^{inc}=\pi/2$. (a) The solid curve depicts $\|\mathbf{v}\|$, and the dashed curve depicts $\|\mathbf{v}_{noise}\|$; (b) $\mathcal{P}^j\times 10^{-3}$ ($\tilde{\eta}^{43}=1.1$).

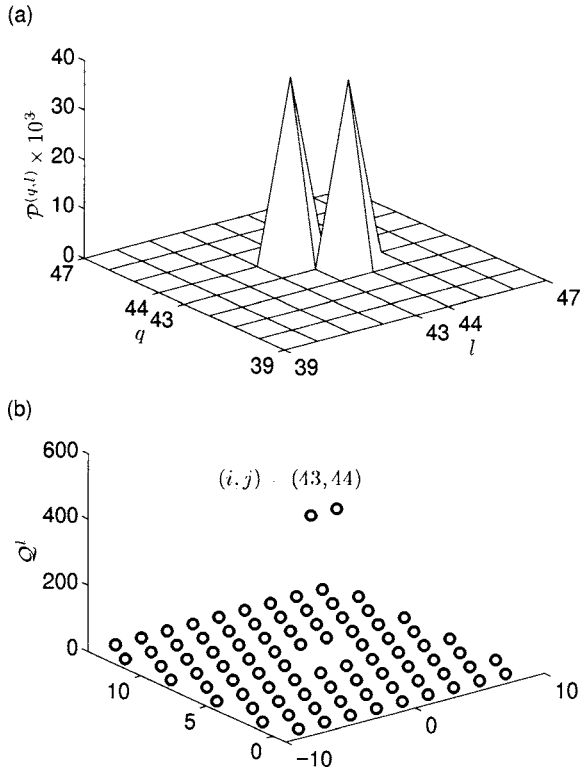

Fig. 8. Crystal with two defects close to each other when $d=2$: $R=0.15$, $\eta^l=1$, and $\theta^{inc}=\pi/2$. (a) $\mathcal{P}^{(q,l)}\times 10^{-3}$ ($\tilde{\eta}^l=1.1$); (b) $\mathcal{Q}^l$.

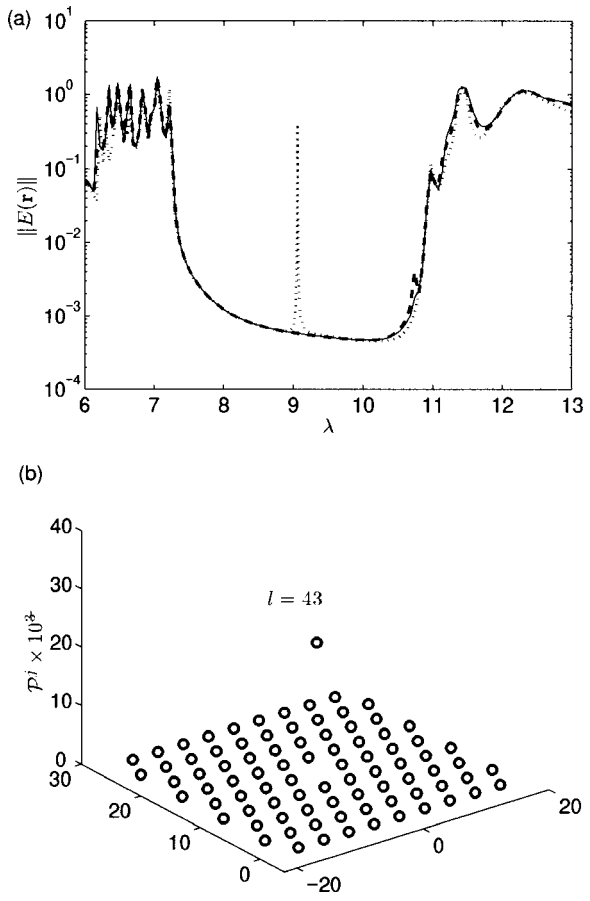

Fig. 9. Crystal with a single defect when $d=4$, $R=0.6$, $\eta=2.9$, and $\theta^{inc}=\pi/2$. (a) Average absolute value of the electric field along a segment lying below the crystal without defect (solid curve), with a single defect $\eta^{43}=1$ (dotted curve), and with a single defect $\eta^{43}=2.8$ (dashed curve) for a wavelength within the bandgap; (b) $\mathcal{P}^j \times 10^{-3}$ for the single defect $\eta^{43}=2.8$ when $\lambda=80$.

Born approximation are then no longer valid. Yet, whenever a small change of the optical index of the central cylinder is assumed, no particular effect is noticed within the bandgap [refer to Fig. 9(a)]. For example, this type of defect could be due to a discrepancy in the optical index of that particular cylinder during the manufacturing of the crystal, or it could be the first manifestation of its deterioration. But such a kind of defect can hardly be retrieved within the frequency range of the bandgap.

Our algorithm is applied onto synthetic data when configurations FSC and 43rd DFSC with $\eta^{43}=2.8$ are illuminated by a low-frequency incident plane wave such that $\lambda=80$. This wavelength is determined by keeping $k\eta R$ constant with the previous case $\lambda=20$ and $R=0.15$. In Fig. 9(b) $\mathcal{P}^j$ is displayed, which shows that the defect is occurring at the location of the 43rd cylinder. The reconstructed optical index is $\Re(\tilde{\eta}^{43})=2.80012$, which is rather a perfect value. That is, the algorithm, though it does not consider the frequency(ies) at which the largest modifications occur, still enables us to quickly retrieve a simple defect that has no particular impact in the bandgap.

5. CONCLUSION

The simple tomographic algorithm described herein appears as a first step in the monitoring of structured materials like PCs. Use of the specific Green's function together with the first-order Born approximation enables us to localize and characterize simple defects consisting in the absence of cylinders or in the identical modification of the optical index of cylinders in finite-sized PCs. Several results exhibit a possible retrieval of two defects beyond the Rayleigh criterion. The dependence of h^l on the angle of incidence of the plane wave solicitation, as well as its dependence on the defect location, remains a challenge. Of particular interest should be the extension of the proposed algorithm to localization and characterization of other defect types consisting, for example, in a modification of the position of a cylinder, of the radius of a cylinder, or of its shape, using the specific Green's function as calculated outside the cylinders. The algorithm can also be used as a first step in an iterative solution scheme, either an iterative Born or modified Born scheme, or a scheme consisting in applying a higher and higher frequency at each iteration.

Various difficulties would arise if the low-frequency approximation was no longer valid, which is the case for usual PCs at the location of the bandgap (their frequency band of operation). In this case, a rather similar algorithm can be set up by accounting for the higher order of the useful coefficients of the scattered fields. This could largely increase the computational time, and consequently the time needed to solve the inverse problem, as this time is very brief for any low-frequency excitation. Thus, particular attention must be given to the computational time/accuracy ratio of the result.

On the other hand, we have exhibited a realistic case in which a defect consisting in a small change of the optical index of a cylinder has no visible impact within the frequency of the bandgap but can be accurately recovered in a simple fashion, when solicited at a low frequency, via the algorithm advocated herein. These results are in effect quite interesting in our opinion, since they show that the frequency range of interest differs depending upon the objective: Frequencies within the bandgap are those at which the most interesting features of PCs in terms of physical properties and practical applications occur, while other frequency ranges should be examined for monitoring and early detection of defects.

REFERENCES

1. J. D. Joanopoulos, R. D. Meade, and J. N. Winn, *Photonic Crystals: Molding the Flow of Light* (Princeton U. Press, 1995).
2. E. Yablonovitch, "Photonic band-gap structures," J. Opt. Soc. Am. B **10**, 283–295 (1993).
3. S. Enoch, B. Gralak, and G. Tayeb, "Enhanced emission with angular confinement form photonic crystals," Appl. Phys. Lett. **81**, 1588–1590 (2002).
4. E. R. Brown, C. D. Parker, and E. Yablonovitch, "Radiation properties of a planar antenna on a photonic-crystal substrate," J. Opt. Soc. Am. B **10**, 404–407 (1993).
5. Ph. Lalanne and A. Talneau, "Modal conversion with artificial materials for photonic-crystal waveguides," Opt. Express **10**, 354–359 (2002).
6. S. Foteinopoulou and C. M. Soukoulis, "Negative refraction and left-handed behaviour in two-dimensional photonic crystals," Phys. Rev. B **67**, 235107 (2003).
7. A. A. Asatryan, K. Busch, R. C. McPhedran, L. C. Botten, C. M. de Sterke, and N. A. Nicorovici, "Two-dimensional

Green tensor and local density of states in finite-sized two-dimensional photonic crystals," Waves Random Media **13**, 9–25 (2005).
8. K. M. Ho, C. T. Chan, and C. M. Soukoulis, "Existence of a photonic gap in periodic dielectric structures," Phys. Rev. Lett. **65**, 3152–3155 (1990).
9. K. M. Leung, "Defect modes in photonic band structures: a Green's function approach using vector Wannier functions," J. Opt. Soc. Am. B **10**, 303–306 (1993).
10. G. Tayeb and D. Maystre, "Rigorous theorical study of finite-size two-dimensional photonic crystals doped by microcavity," J. Opt. Soc. Am. A **12**, 3323–3332 (1993).
11. L. C. Botten, R. C. McPhedran, N. A. Nicorovici, A. A. Astryan, C. M. de Sterke, P. A. Robinson, K. Busch, G. H. Smith, and T. N. Langtry, "Rayleigh multipole methods for photonic crystals calculation," Prog. Electromagn. Res. **41**, 21–60 (2003).
12. D. Felbacq, G. Tayeb, and D. Maystre, "Scattering by a random set of parallel cylinders," J. Opt. Soc. Am. A **11**, 2526–2538 (1994).
13. J.-P. Groby, L. de Ryck, P. Leclaire, A. Wirgin, W. Lauriks, R. P. Gilbert, and Y. S. Xu, "Use of specific Green's function for solving direct problems involving a heterogeneous rigid frame porous medium slab solicited by acoustic waves," Math. Methods Appl. Sci. **30**, 91–122 (2007).
14. E. Ozbay, I. Bulu, K. Aydin, H. Caglayan, and K. Guven, "Physics and applications of photonic crystals," Photonics Nanostruct. Fundam. Appl. **2**, 87–95 (2004).
15. A. Sentenac, P. C. Chaumet, and K. Belkebir, "Beyond the Rayleigh criterion: grating assisted far-field optical diffraction tomography," Phys. Rev. Lett. **97**, 243901 (2004).
16. W. C. Chew, *Waves and Fields in Inhomogeneous Media* (IEEE, 1995).
17. I. S. Gradsteyn and I. M. Ryzhik, *Table of Integrals, Series, and Products* (Academic, 2000).
18. H. Ammari, E. Iakovleva, and D. Lesselier, "Two numerical methods for recovering small inclusions for the scattering amplitude at a fixed frequency," SIAM J. Sci. Comput. (USA) **27**, 130–158 (2005).
19. P. W. Barber and S. C. Hill, *Light Scattering by Particles: Computation Methods* (World Scientific, 1990).
20. G. Lerosey, J. de Rosny, A. Tourin, and M. Fink, "Focusing beyond the diffraction limit with far-field time reversal," Science **315**, 1120–1122 (2007).